Zinc-Based Spinel Cathode Materials for Magnesium Rechargeable Batteries: Toward Reversible Spinel–Rocksalt Transition

Journal:	*Journal of Materials Chemistry A*
Manuscript ID	TA-ART-03-2019-002281.R1
Article Type:	Paper
Date Submitted by the Author:	02-Apr-2019
Complete List of Authors:	Shimokawa, Kohei; Tohoku University Institute for Materials Research Atsumi, Taruto; Nagoya Institute of Technology, Department of Materials Science and Engineering harada, maho; Nagoya Institute of Technology, Department of Materials Science and Engineering Ward, Robyn; National Institute for Materials Science Nakayama, Masanobu; Nagoya Institute of Technology, Department of Materials Science and Engineering Kumagai, Yu; Tokyo Institute of Technology, Materials Research Center for Element Strategy Oba, Fumiyasu ; Tokyo Institute of Technology, Laboratory for Materials and Structures Okamoto, Norihiko; Tohoku University Institute for Materials Research Kanamura, Kiyoshi; Tokyo Metropolitan University Ichitsubo, Tetsu; Tohoku Daigaku, Institute for Materials Research

SCHOLARONE™
Manuscripts

Journal of Materials Chemistry A

Stabilizing spinel structure by Zn preferring tetrahedral environment significantly improves the reversibility in the spinel–rocksalt transition with Mg insertion/extraction (20 words)
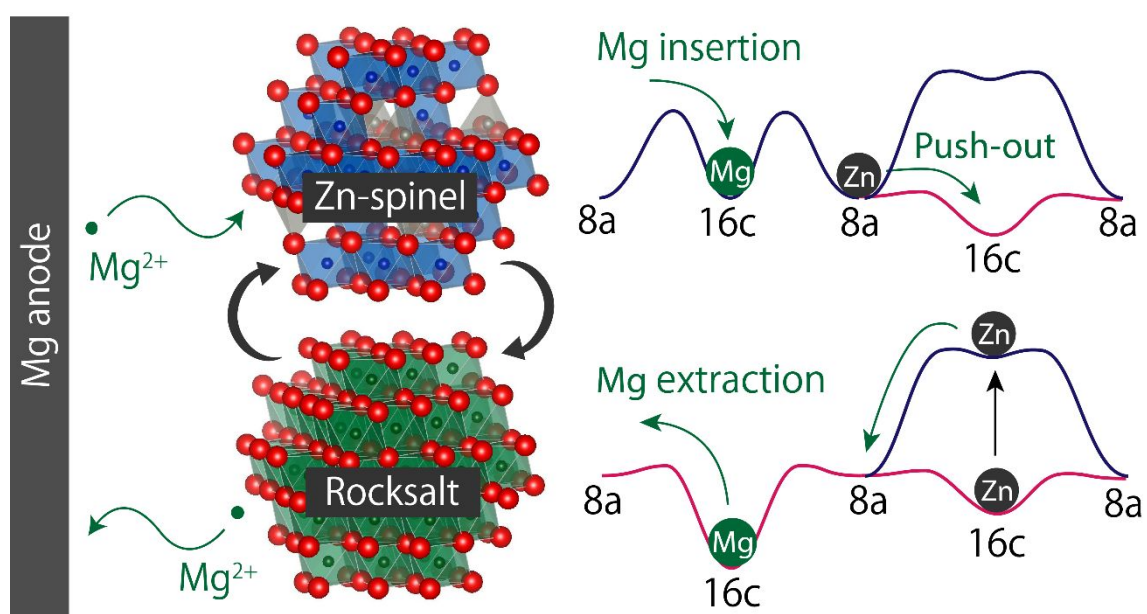
ARTICLE TYPE

Zinc-Based Spinel Cathode Materials for Magnesium Rechargeable Batteries: Toward Reversible Spinel–Rocksalt Transition[†]

Kohei Shimokawa,[*a] Taruto Atsumi,[b] Maho Harada,[b] Robyn E. Ward,[c] Masanobu Nakayama,[bc] Yu Kumagai,[d] Fumiyasu Oba,[ce] Norihiko L. Okamoto,[a] Kiyoshi Kanamura,[f] and Tetsu Ichitsubo[*a]

Spinel-to-rocksalt transition with Mg insertion into spinel oxides upon discharge can be utilized as a cathode reaction for magnesium rechargeable batteries. However, the formation of a resulting robust rocksalt phase can be harmful to the cyclability, in that it is sluggish to revert to its original spinel structure. In this work, we show that the inverse "rocksalt-to-spinel" transition can be facilitated upon charge by stabilizing the spinel structure with Zn preferring tetrahedral environment. Our ab-initio calculation study substantiates that Zn-based spinel oxides (space group #227) favor a normal-spinel configuration owing to a covalency of Zn–O in the tetrahedral 8a site, and a cation disordering or migration from 8a to 16c sites tends to be unfavored in terms of thermodynamics and kinetics. Based on this theoretical prediction, we show experimentally that such a stabilized normal spinel structure (i.e., $ZnCo_2O_4$ and $ZnFe_2O_4$) consequently allows the reversible spinel–rocksalt transition upon charge and discharge processes. Furthermore, the volume change of $ZnFe_2O_4$ in discharge/charge is much smaller than that of Co-based spinel oxides, which can provide a nearly zero-strain cathode material consisting of abundant elements.

INTRODUCTION

Toward future sustainable society, there is a growing demand for large-scale batteries applying to electric vehicles and stationary energy storage systems. Although lithium ion batteries[1] are currently used for these purposes, it is imperative to enhance the energy density in parallel to the improvement of battery safety. Magnesium rechargeable batteries (MRBs) have been one of promising candidates for next-generation batteries.[2] A remarkable merit is that Mg can deposit with nondendritic formation unlike Li,[3,4]

which allows us to use Mg metal itself as the anode material with a high capacity (2205 mAh g^{-1}) and a low electrode potential (-2.4 V vs. SHE).[5] In addition, MRBs are suitable for large-scale batteries since Mg is one of the highest abundant and non-toxic chemical elements. However, the main bottleneck in the development of MRBs is that reversible Mg insertion/extraction on the cathode is difficult due to the sluggish Mg diffusion inside host materials. Recently, it has been revealed that large amounts of Mg can be inserted into several Mg-based spinel oxides (e.g., $MgCo_2O_4$) at elevated temperatures around 150 °C, which proceeds in the two-phase reaction with the spinel and rocksalt phases.[6] Although high-temperature operation is somewhat unsuitable for mobile appliances, MRBs have significant advantages in terms of their safety and abundant resources, which are indispensable for scaling-up of batteries; in such large-scale systems, their temperature can be controlled by using electric heaters or exhaust heat. To exploit the capability of spinel–rocksalt transition materials (SRTMs), it is necessary to establish general guidelines for designing spinel oxides to control of the structural stability, reversibility, and coherent strain, etc.

Figure 1 illustrates the typical structural difference between spinel (AB_2O_4) and rocksalt ($MgAB_2O_4$) phases in SRTMs; the space group #227 ($Fd\bar{3}m$), which the spinel structure belongs

[a] *Institute for Materials Research, Tohoku University, 2-1-1 Katahira Aoba-ku Sendai 980-8577, Japan. E-mail: shimokawa.kohei@imr.tohoku.ac.jp; tichi@imr.tohoku.ac.jp*

[b] *Frontier Research Institute for Materials Science (FRIMS), Department of Materials Science and Engineering, Nagoya Institute of Technology, Gokiso-cho, Showa-ku, Nagoya, Aichi 466-8555, Japan*

[c] *MaDiS/CMi², National Institute of Materials Science (NIMS), 1-2-1, Sengen, Tsukuba, Ibaraki 305-0047, Japan*

[d] *Materials Research Center for Element Strategy, Tokyo Institute of Technology, Yokohama 226-8503, Japan*

[e] *Laboratory for Materials and Structures, Institute of Innovative Research, Tokyo Institute of Technology, Yokohama 226-8503, Japan*

[f] *Department of Applied Chemistry, Tokyo Metropolitan University, 1-1 Minami-Osawa, Hachioji, Tokyo 192-0357, Japan*

[†] Electronic Supplementary Information (ESI) available: [details of any supplementary information available should be included here]. See DOI: 10.1039/b000000x/
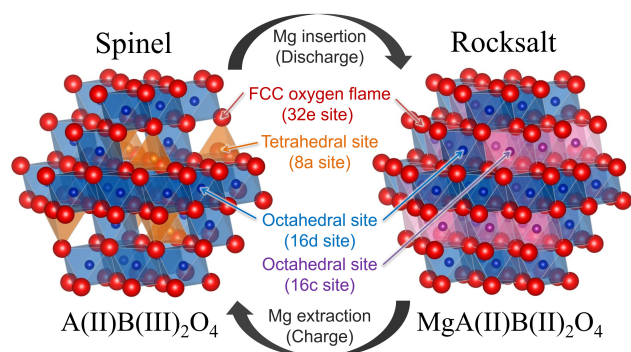
Fig. 1 The typical structural change with Mg insertion/extraction in spinel–rocksalt transition materials (SRTMs). Mg insertion into 16c vacant sites causes pushing out of the cations located at 8a sites into other 16c vacant sites to form the rocksalt structure. The Wyckoff sites in both structures are denoted based on the space group #227.

to, is also adopted to the rocksalt structure in order to make it easy to compare the two structures. First of all, both of the structures have the same face-centered cubic (fcc) oxygen flame (32e), whereas the sites occupied by cations are different. In the spinel structure, there are both tetrahedral (8a) and octahedral (16d) sites for cations to occupy, while the other octahedral (16c) sites are vacant. On the other hand, in the rocksalt structure, all octahedral sites (16c and 16d) are homogenously occupied by cations to achieve the closer packing. According to the previous report,[6] by the Mg insertion into 16c vacant sites in the spinel structure, the cations at 8a sites pushed out to other 16c vacant sites, resultingly, to form the rocksalt structure. Here it deserves to note that, based on the above mechanism, the spinel oxides for MRBs need no Mg elements in the initial structure, and we can begin with the discharge process with Mg metal anode. Furthermore, Mg-based spinel oxides would suffer from the formation of a robust and insulative MgO-like rocksalt phase during cycling; actually, a rapid capacity fade was observed for $MgCo_2O_4$ within a few cycles[6,7] (although the anodic limit in the electrochemical widow is also an issue). Therefore, exploring Mg-free SRTMs is an urgent task for developing high-performance MRBs.

In this work, focusing on the feature that Zn prefers tetrahedral configuration in spinel oxides, we demonstrate theoretically and experimentally that Zn-based spinel oxides exhibit a markedly improved reversibility in the spinel–rocksalt transition. Specifically, we have chosen Co and Fe as transition elements in the Zn-based spinel oxides, because we have intensively investigated $MgCo_2O_4$ and $MgFe_2O_4$ in the previous work.[6] First, by means of ab-initio computational methods, we investigate the roles of Zn in SRTMs, i.e., to what degree Zn stabilizes the spinel host structure from the viewpoints of thermodynamics and kinetics. Next, compare with Ni-based spinels (e.g., $NiCo_2O_4$), where Ni is a well-known element to favor the octahedral site unlike Zn, we experimentally show the superiority of Zn-based spinel oxides in terms of the electrochemical cyclability. In addition, we demonstrate that $ZnFe_2O_4$ shows markedly improved cyclability with small volume strain in discharge/charge. This work provides crucial guidelines for designing spinel oxides towards MRB cathode materials.

RESULTS AND DISCUSSION

Computational Analysis

Facilitating cation migration from octahedral 16c to tetrahedral 8a sites would play a key role for inverse rocksalt-to-spinel transition. We focused Zn^{2+} as a candidate for the cation to sit at the tetrahedral 8a sites in the spinel oxides, because it is empirically known that Zn^{2+} strongly prefers tetrahedral coordination in oxides. In fact, ZnO readily forms the wurtzite structure, where Zn^{2+} occupies tetrahedral sites. Besides, also in spinel oxides, Zn^{2+} preferentially occupies tetrahedral 8a sites instead of octahedral 16d sites.[8–13] To clarify the properties and the origin of the strong tetrahedral preference of Zn^{2+} in oxides, we performed computational study on spinel $ZnCo_2O_4$ and $MgCo_2O_4$ as typical examples. We firstly compared the site stability of 8a and 16d sites between $MgCo_2O_4$ and $ZnCo_2O_4$ spinel compounds, using density functional theory (DFT) based computational approaches. A genetic algorithm (GA) approach with DFT + U calculations was used to determine the most stable cation configuration, i.e. Mg (Zn) and Co arrangement between the 8a and 16d sites in $MgCo_2O_4$ ($ZnCo_2O_4$), while minimizing the total energy. A conventional cubic spinel cell consisting of 56 atoms was used for the crystal structure inputs, i.e. $Mg_8Co_{16}O_{32}$ or $Zn_8Co_{16}O_{32}$. The details of the GA approach are detailed elsewhere.[14] The GA optimized structures for both $MgCo_2O_4$ and $ZnCo_2O_4$ were normal spinels, i.e. the divalent cation Mg^{2+} or Zn^{2+} occupying the 8a tetrahedral sites and trivalent Co^{3+} ions in the 16d octahedral sites. The detailed structure parameters are listed in Tables S1 and S2. These results differ from previous experimental studies, where the occupancy of Co ions at the 8a site was calculated to be 0.475 and 0.20 in $MgCo_2O_4$ or $ZnCo_2O_4$, respectively.[10,15] This difference may come from the fact that DFT + U driven GA optimization corresponds to synthesis at zero Kelvin (this is discussed later). Because the energy differences between the first and second most stable configurations are only 0.11 eV/f.u. and 0.20 eV/f.u. for $MgCo_2O_4$ and $ZnCo_2O_4$, respectively, it is expected that Mg/Co mixing between the 8a and 16d sites in $MgCo_2O_4$ occurs more easily at elevated temperature than Zn/Co mixing in $ZnCo_2O_4$ due to the entropic effect.

To quantitatively evaluate the cation configuration at elevated temperatures, DFT derived Monte Carlo simulation with cluster expansion technique was used (see details in Supporting Section S1). The heat capacities for both compounds at low temperatures (300 to ~600 K) are unchanged showing no Co occupation at 8a sites (Figure 2a), indicating the formation of a normal spinel, for both compositions in accordance with the GA derived structures. Increase of the heat capacity corresponds to the increase of cation disorder as shown in the left and the right panels of Figure 2a. The onset temperature of this energy increase in $MgCo_2O_4$ is lower than that in $ZnCo_2O_4$, indicating that the cation disordering in $MgCo_2O_4$ is more likely than in $ZnCo_2O_4$. This is consistent with the previously mentioned experimental reports.[10,15] Since the occupation of high-valency Co ions at 8a tetrahedral sites can block the migration pathway of the divalent ion 8a–16c-vacancy–8a diamond network (percolation threshold is ~0.55 of Co occupation at 8a site),[16] $ZnCo_2O_4$ would be advan-
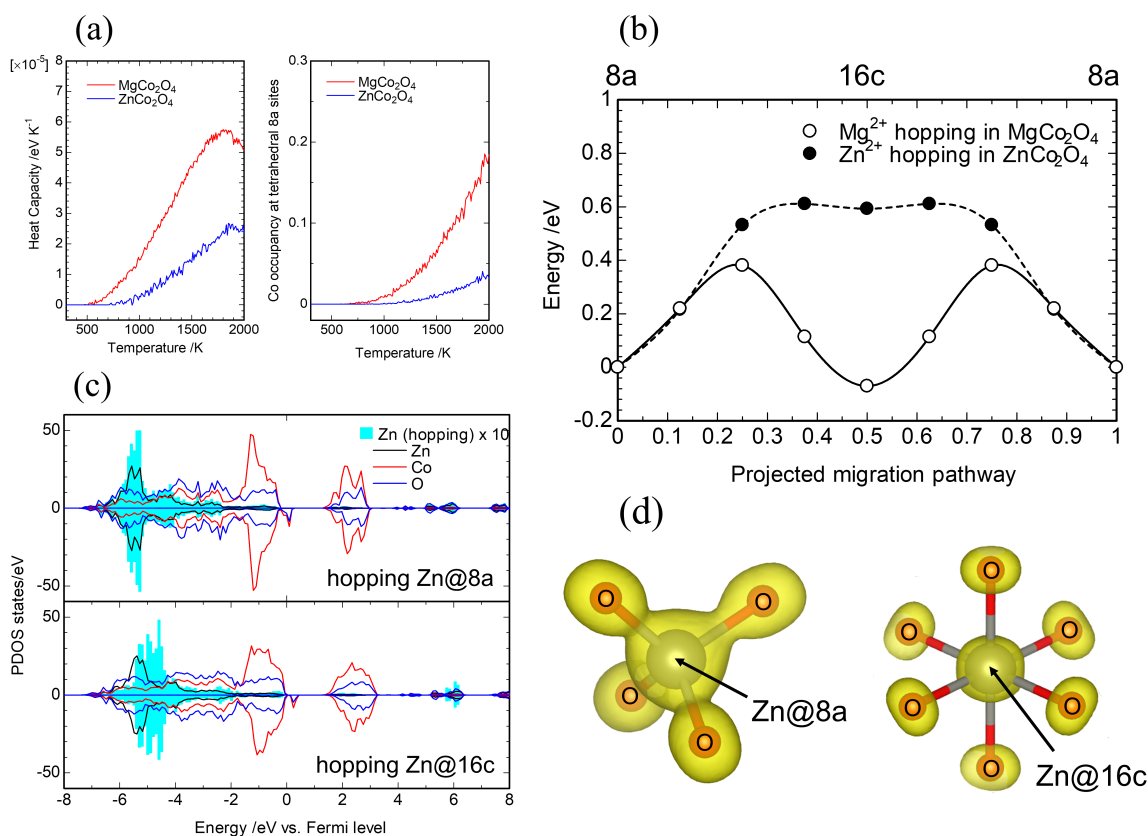
Fig. 2 (a) Variation of Monte Carlo simulation derived heat capacity (left) and Co occupancy at tetrahedral 8a sites (right) as a function of temperature for $MgCo_2O_4$ and $ZnCo_2O_4$. (b) Energy profile of the Mg^{2+} jump in $Mg_7Co_{16}O_{32}$ (empty circle) and Zn^{2+} jump in $Zn_7Co_{16}O_{32}$ (solid circle) from 8a site (0) to vacant 8a site (1) via the 16c site (0.5) calculated by the NEB method with DFT + U. Energy is set at zero, when the divalent cation is in the 8a site. (c) Partial density of states (PDOS) for $ZnCo_2O_4$. Upper and lower panels correspond to the electronic structures for a hopping Zn at tetrahedral 8a and octahedral 16c sites in $ZnCo_2O_4$, respectively. Light blue bars in panels show the PDOS for hopping Zn ions, magnified by a factor of 10 for visibility purposes. (d) Yellow colored isosurface representing the partial electronic density around a hopping Zn ion at tetrahedral 8a site (left) and octahedral 16c site (right) in the energy range -6.5 to -5.0 eV and -6.0 to -4.0 eV against Fermi level, respectively.

tageous in terms of diffusion pathway network of divalent cation migration as it disorders less at higher temperatures.

The nudged elastic band (NEB) method was used to calculate the activation barriers for Mg^{2+} and Zn^{2+} divalent cations between 8a tetrahedral sites in $A_7Co_{16}O_{32}$ (A = Mg, Zn), where one 8a site is vacant. As shown in Figure 2b, Mg^{2+} produces a double potential barrier between the two 8a sites while Zn^{2+} produces a higher single potential barrier, which is consistent with a previous report.[17] The trajectory for both the Mg^{2+} and Zn^{2+} jump is straightforward along [111] direction between two tetrahedral 8a sites through the octahedral 16c vacancy site. The results of the trajectories agree with previous computations for the Li hop in the $LiMn_2O_4$ and $LiCoO_2O_4$ systems.[18] The migration energy—the energy difference between the pathway maximum and minimum—is 452 meV and 612 meV for the Mg^{2+} and Zn^{2+} jump, respectively. The calculated migration energies are sufficiently small for the divalent cation migration, being suitable for battery usage at room temperature, if one prepares sufficiently small particles as described in Supporting Section S2 and Supporting Table S3. Although there is a large difference in energy profile shape between $MgCo_2O_4$ and $ZnCo_2O_4$, the ionic radius of Mg^{2+} (Mg^{2+}_{tet}: 0.57 Å,

Mg^{2+}_{oct}: 0.72 Å) is almost the same as that of Zn^{2+} (Zn^{2+}_{tet}: 0.60 Å, Zn^{2+}_{oct}: 0.74 Å).[19] Actually, the interatomic distance between hopping Mg^{2+} or Zn^{2+} ion and nearest neighbor O or Co ions indicating no significant difference for divalent cation hops in $MgCo_2O_4$ and $ZnCo_2O_4$ (Figure S2). Therefore, the difference in energy profile shown in Figure 2b must be due to the other factors, such as electronic structure, and so on. To understand what causes this difference, we calculated the partial density of states (PDOS) of $MgCo_2O_4$ and $ZnCo_2O_4$ for DFT-NEB calculations, where hopping divalent cations were located at tetrahedral 8a and octahedral 16c sites. In $MgCo_2O_4$, there are no states derived from the Mg ion in the vicinity of Fermi level, indicating pure ionic bonding (Figure S3). On the other hand, Zn 3d band formation is visible at a valence state near to Fermi level (Figure 2c). For the hopping Zn^{2+} ions, the Zn 3d band shifts from ~ -5.5 eV at the 8a site to ~ -5.0 eV at the 16c site. The partial electronic charge density distribution for corresponding energy level of hopping Zn^{2+} ions in $ZnCo_2O_4$ are shown in Figure 2d. The overlap of electron density with the nearest neighbor O ions is observed for Zn^{2+} ion at 8a tetrahedral site, although it is isolated when the Zn^{2+} ion is located at 16c octahedral site. These results indicate that

Zn 3d orbital on the tetrahedral site is strongly interacted with O 2p orbital, and lowering the energy level of the valence band. Nevertheless, since it is difficult to consider the covalent bonding formation with O 2p orbital by only fully filled 3d-shell ($3d^{10}$ electronic configuration), we should take into account the effects of Zn 4s and 4p electrons in addition to 3d electron. But even so, we are sure that Zn^{2+} ion sit preferably at the tetrahedral site forming the covalent bond with O 2p orbital, whereas Zn^{2+} ion at the octahedral site is relatively ionic.

Experimental Characterization of $A(Co/Fe)_2O_4$ (A = Zn, Ni)

Nanocrystalline powder samples of $ZnCo_2O_4$ and $ZnFe_2O_4$ (hereafter referred to as $Zn(Co/Fe)_2O_4$) were synthesized by an inverse coprecipitation method.[15] The primary particle size of each sample was found to be ∼10 nm (Figure S5), by high-angle annular dark-field (HAADF) scanning transmission electron microscopy (STEM). It should be noted that, due to the sluggish diffusion of Mg^{2+}, preparing small primary particles by low-temperature calcination is critical for facilitating Mg insertion/extraction. We also examined Ni-based spinel oxides for comparison, because Ni has the opposite nature to Zn in that it generally prefers octahedral 16d sites in spinel oxides.[20–26] Figure 3 shows the obtained XRD profiles of $A(Co/Fe)_2O_x$ (A = Zn, Ni) after calcination at 350 °C. The obtained XRD profiles can be assigned to the spinel structure (compare with the ICSD profile of $ZnFe_2O_4$ in Figure 3) except for the Ni–Fe complex, whose profile is obviously different from that of the ideal spinel structure. This is probably because Ni stabilizes the rocksalt structure due to its preference for octahedral coordination. As stated before, the spinel and rocksalt structures are basically similar in terms of anion configuration, although cation sites are slightly different (Figure 1). Thus, XRD patterns of the spinel and rocksalt structures can also be seen as similar. In particular, the diffraction peaks of 111, 200, and 220 in the rocksalt structure (e.g., denoted as 111_R) corresponds to those of 222, 400, and 440 in the spinel structure (e.g., denoted as 222_S), respectively, whereas the other peaks for the spinel structure are absent for the rocksalt structure (see ICSD profiles of MgO and $ZnFe_2O_4$ in Figure 3). The profile for the obtained Ni–Fe complex suggests that it has an in-between structure of the spinel and rocksalt, because the intensity of the peaks of other than 222_S, 400_S and 440_S are markedly decreased compared to those of the ideal spinel structure.

As for $ZnFe_2O_4$, there is no significant difference between the experimental XRD profile and that of the ICSD data. In the light of the fact that Ni-based compound does not show the fine spinel structure, this results reflects that Zn play a role of spinel-phase stabilizer. It was reported that although most Fe-based spinel oxides including $NiFe_2O_4$ tends to form inverse spinel structures (e.g., $[Fe^{3+}_1]_{8a}[Ni^{2+}_1 Fe^{3+}_1]_{16d}O_4$),[23–26] $ZnFe_2O_4$ exceptionally prefers normal spinel structure.[8,9] The cation distribution of the synthesized nanocrystals can be estimated by comparing the intensity ratio of I_{400_S}/I_{220_S}, which is known to be sensitive for the cation distribution (8a and 16d) in spinel oxides.[27,28] The values of I_{400_S}/I_{220_S} determined from the obtained profiles of $ZnFe_2O_4$ and $ZnCo_2O_4$ are within 0.50–0.55 in both cases, which suggests
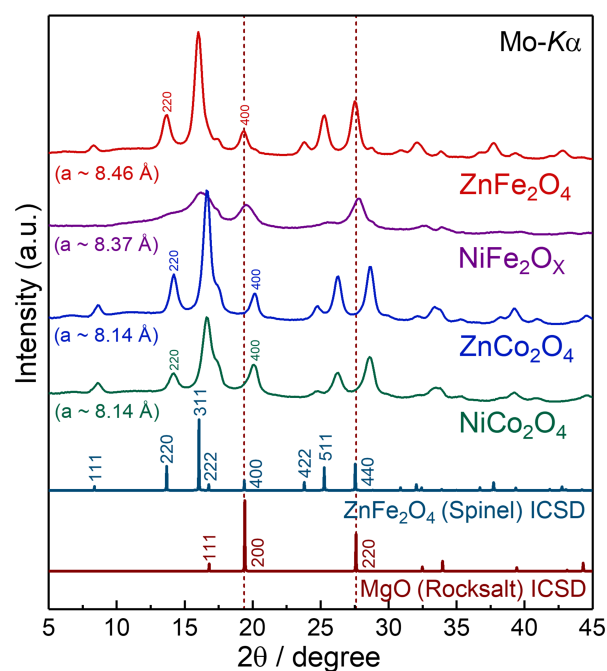

Fig. 3 X-ray diffraction profiles obtained for the synthesized $A(Co/Fe)_2O_4$ (A = Zn, Ni) nanocrystalline powders. The lattice size of $ZnFe_2O_4$ is similar to that of rocksalt MgO, while Co-based spinel oxides have much smaller lattice constants.

that Zn^{2+} ions mainly occupy 8a sites by comparing with the results of simulation (in the case of $ZnFe_2O_4$, ca. 0.4 for normal spinel and ca. 0.9 for inverse spinel, as shown in Figure S6). As for $NiCo_2O_4$, I_{400_S} is larger than I_{220_S} in the obtained profile (i.e., $I_{400_S}/I_{220_S} > 1$); however, such an intensity ratio cannot be reproduced in any cation distribution in the spinel structure without any defects (Figure S6). Namely, the obtained nanocrystals of $NiCo_2O_4$ would contain rocksalt-like defects intrinsically, as also reported for Mn-based spinel oxides.[29]

The lattice misfit between the spinel and rocksalt phases should be considered in designing SRTMs. It can be tentatively estimated by comparing the lattice constants of the synthesized spinel oxides and that of rocksalt MgO, because the lattice size of the rocksalt phase after Mg insertion is expected to get closer to that of MgO. The lattice constants of both of the Co-based compositions are determined to be ca. 8.14 Å from the obtained XRD profiles. Meanwhile, the lattice constant of MgO is known to be ca. 4.21 Å (i.e., 8.42 Å for comparing with spinel oxides).[30] Thus, as shown in Figure 3, there is a relatively large difference between the angle of the 440_S peaks of Co-based spinel oxides and that of the 220_R peak of MgO. On the other hand, the obtained lattice constant of $ZnFe_2O_4$ (ca. 8.46 Å) is much larger than those of the Co-based compositions, but it is comparable with the value for MgO (ca. 8.42 Å). Actually, the volume change of $ZnFe_2O_4$ with Mg insertion/extraction is much smaller than that of $ZnCo_2O_4$ (this will be shown in the later section). To investigate the dependence of the composition on the lattice size, XRD measurements were carried out for several spinel oxides containing both Fe and Co. As a result, it was revealed that the lattice constant was systemati-
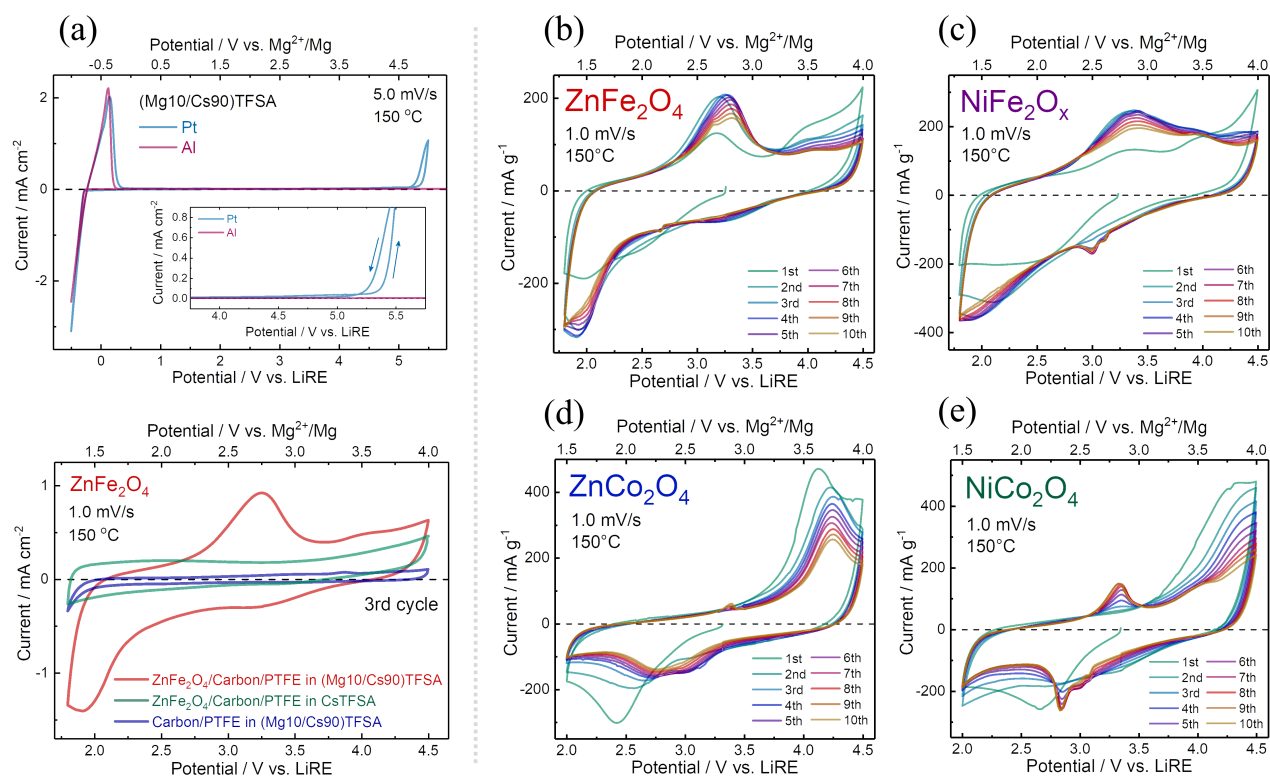
Fig. 4 (a) Electrochemical window of (Mg10/Cs90)TFSA ionic liquid at 150 °C on Pt and Al foils (upper), where Cs deposition/dissolution occurs at low potential, and cyclic voltammograms of $ZnFe_2O_4$ in CsTFSA with/without $Mg(TFSA)_2$ and also of a blank electrode for comparison (lower). (b–e) Cyclic voltammograms of several spinel oxides ($ZnFe_2O_4$, $NiFe_2O_x$, $ZnCo_2O_4$, and $NiCo_2O_4$) in (Mg10/Cs90)TFSA at 150 °C with a scan rate of 1 mV s^{-1}.

cally increased with the increase of the molar ratio of Fe/Co (Figure S7). This is consistent with the fact that the ionic radius of Fe^{3+} is larger than that of Co^{3+} (Fe^{3+}_{oct} in high-spin state: 0.645 Å, Co^{3+}_{oct} in low-spin state: 0.545 Å),[19] where it should be noted that Co^{3+} tends to have low spin state in spinel oxides.[31,32]

Electrochemical properties of the synthesized spinel oxides were examined with (Mg10/Cs90)TFSA ionic liquid at elevated temperature of 150 °C to facilitate Mg^{2+} diffusion. Because Mg metal is known to be passivated in the presence of TFSA anions,[33,34] a Li^+/Li reference electrode system (hereafter referred to as "LiRE") was employed by separating it from the main bath with a ceramic filter. Figure 4a (upper) shows cyclic voltammograms (CVs) in (Mg10/Cs90)TFSA electrolyte at 150 °C obtained by using Pt and Al foils. The deposition/dissolution of Cs instead of Mg was observed at low potential on both electrodes, because the electrodeposition of Mg hardly occurs in this electrolyte. Nevertheless, it has been proven that $Mg(TFSA)_2$ is ionized in the (Mg10/Cs90)TFSA electrolyte,[35] and the redox potential of Mg^{2+}/Mg in the electrolyte has been estimated to be ca. 0.5 V vs. LiRE in the previous report.[6] Anodic current due to the decomposition of TFSA anion was observed at ~5 V vs. LiRE for Pt electrode. Such a wide electrochemical window even at elevated temperatures is appropriate for evaluating high-potential cathode materials. Anodic dissolution of Al was not observed even at high potential around 5 V, indicating that the surface of Al is favorably passivated in the electrolyte. Thus, Al was used as current collector for the following CV measurements. The lower panel in Fig-

ure 4a shows CVs of $ZnFe_2O_4$ in (Mg10/Cs90)TFSA and in pure CsTFSA, and also CV of a blank electrode (only carbon and PTFE binder) for comparison. Obvious redox peaks were observed at ~1.5/2.7 V vs. Mg^{2+}/Mg for the CV profile in (Mg10/Cs90)TFSA, although they were absent in pure CsTFSA electrolyte. Thus, it is considered that Mg insertion/extraction into/form $ZnFe_2O_4$ occurs with the valence change of Fe^{2+}/Fe^{3+}. The redox peaks become broader with the increase of the scan rate (Figure S8), indicating the relatively slow kinetics of Mg insertion/extraction into/from spinel host. Incidentally, another redox reaction was observed at the higher potentials of ~3.0/3.7 V vs. Mg^{2+}/Mg, where Fe ions possibly oxidized to higher than trivalent Fe^{3+} in charged state due to the slight extraction of Zn from $ZnFe_2O_4$ as is discussed later.

Figures 4b–4e show the CVs of the spinel oxides at 150 °C for 10 cycles with a scan rate of 1 mV s^{-1}. In both Fe-based and Co-based composites, Zn-containing spinel oxides show facile redox reactions compared to Ni-containing ones. The redox peaks become broad for $NiFe_2O_x$ compared with the case for $ZnFe_2O_4$, which is likely because it has defective structure with low crystallinity. The redox potentials become approximately 1 V higher for Co-based composites compared with Fe-based ones; in particular, the redox peaks that probably correspond to the valence change of Co^{2+}/Co^{3+} were observed at ~2.5/3.7 V vs. Mg^{2+}/Mg. In the case of $NiCo_2O_4$, it is considered that not only Co but also Ni can change its valence, so the valence states of Ni and Co after discharge/charge were investigated by using X-ray absorption

Table 1 Predicted equilibrium redox potentials[a] in the spinel–rocksalt transition[b] by *ab initio* calculation. This includes the data of Mg-containing spinel oxides from the previous report (Ref. 6). The potential is mainly determined by the valence changes of B cations (Fe^{2+}/Fe^{3+} or Co^{2+}/Co^{3+}), but slightly affected by the properties of A cations (Zn^{2+}, Mg^{2+} or Ni^{2+}).

spinel oxides (AB_2O_4)	spinel–rocksalt transition	AO structure	*ab initio*	experimental (1st cycle)
$ZnFe_2O_4$	$ZnFe_2O_4$(spinel) + Mg = $MgZnFe_2O_4$(rocksalt)	ZnO: wurtzite	1.6 V	2.1 V
$MgFe_2O_4$	$MgFe_2O_4$(spinel) + Mg = $Mg_2Fe_2O_4$(rocksalt)	MgO: rocksalt	1.7 V	2.2 V
$ZnCo_2O_4$	$ZnCo_2O_4$(spinel) + Mg = $MgZnCo_2O_4$(rocksalt)	ZnO: wurtzite	2.9 V	2.8 V
$MgCo_2O_4$	$MgCo_2O_4$(spinel) + Mg = $Mg_2Co_2O_4$(rocksalt)	MgO: rocksalt	3.0 V	2.9 V
$NiCo_2O_4$	$NiCo_2O_4$(spinel) + Mg = $MgNiCo_2O_4$(rocksalt)	NiO: rocksalt	3.0 V	3.0 V

[a] The unit of voltage is V vs. Mg^{2+}/Mg. [b] AB_2O_4(spinel) + Mg $\Leftrightarrow$ $MgAB_2O_4$(rocksalt)

near edge structure (XANES) spectroscopy (Figure S9). As a result, it was suggested that the charge compensation was mainly achieved by the valence change of Co^{2+}/Co^{3+}. Although the CV profiles of $ZnCo_2O_4$ show little change during the first 10 cycles, a rapid degradation was observed for $NiCo_2O_4$. To determine the causes of the degradation, XRD measurements were carried out for the electrodes after 20 cycles (Figure S10), where the CV measurements were stopped at the charged state (ideally with the spinel phase). Then, it was revealed that an irreversible rocksalt phase was generated during cycling for $NiCo_2O_4$, whereas such a rocksalt phase was not clearly observed for $ZnCo_2O_4$. Although the capacity fade including electrolyte degradation was still observed for Zn-based spinel oxides in long-term cycling (Figure S11), the above-stated results indicate that stabilizing spinel phase by utilizing Zn is significantly effective to improve the reversibility in the spinel–rocksalt transition.

The equilibrium redox potential for each compound in the spinel–rocksalt transition is predicted by *ab initio* calculation. Table 1 lists the obtained potentials of experimental and calculation studies. It is noted that the calculation was conducted by the same way as our previous work,[6] and the values for Mg-containing compositions were taken from there. Experimental values are determined from the CV curves in the first cycle by taking the average of the peak positions of the oxidative and reductive current. The redox potentials of Fe-based and Co-based compositions are calculated to be within 1.6–1.7 and 2.9–3.0 V, respectively. This suggests that the potential is mainly determined by the transition metals whose valence states change in the reaction (i.e., Fe^{2+}/Fe^{3+} or Co^{2+}/Co^{3+}). Actually, the experimental values also follow this trend, although the values for Fe-based compositions are approximately 0.5 V higher than the calculated values. The equilibrium potential slightly varies also depending on the A cations of $A(Co/Fe)_2O_4$. In particular, the potentials of Zn-containing spinel oxides are approximately 0.1 V lower than those of Mg- and Ni-containing ones in both experimental and calculation studies. This would be because Zn intrinsically prefers tetrahedral coordination and consequently stabilizes the spinel structure, while Mg and Ni favor also octahedral coordination as understood from the fact that MgO and NiO form stable rocksalt structures. Namely, stabilizing spinel phase by Zn lowers the driving force for the full-cell reaction ($\Delta G = \mu_{MgAB_2O_4(rocksalt)} - \mu_{AB_2O_4(spinel)} - \mu_{Mg}$), compared with the case of Mg and Ni, which is a trade-off relation for enhancing the reversibility of spinel–rocksalt transition.

Cathode Performance

Figure 5a shows discharge/charge performance of Zn-based spinel oxides at 150 °C with a current density of 10 mA g^{-1}, where the first discharge was performed without any precharge process. The theoretical energy densities of $ZnCo_2O_4$ and $ZnFe_2O_4$ in the spinel-to-rocksalt transition are 216 and 222 mAh g^{-1}, respectively. Because spinel $ZnFe_2O_4$ was successfully synthesized without calcination (Figure S12), this is used to examine the cathode performance in expectation of its smaller particle size. Composite electrodes were prepared by mixing spinel oxides, carbon black and polyvinylidene fluoride (PVdF) binder in a weight ratio of 8:1:1. Cut-off voltages were determined considering redox potentials of each compound and the electrochemical window of the electrolyte; specifically, the charging cut-off voltage of $ZnFe_2O_4$ was limited to 3.8 V vs. LiRE to prevent the redox reaction at higher potentials observed for the CV measurements, and the discharging cut-off voltage was set at 2.0 V vs. LiRE because the reductive decomposition of the electrolyte can occur below it.

As for $ZnCo_2O_4$ (upper panel in Figure 5a), the discharge capacity in the first cycle amounts to approximately 100 mAh g^{-1} with broad plateau-like potential at 2.5–3.0 V vs. LiRE. This behavior is consistent with previous reports on $MgCo_2O_4$,[6,7,34] where the spinel-to-rocksalt transition occurs via the two-phase reaction process. The differential capacity (dQ/dV) plot (upper panel in Figure 5b) shows sharp peaks around 2.8 and 4.0 V vs. LiRE, which indicates that Mg insertion/extraction into/from $ZnCo_2O_4$ also proceeds through a two-phase reaction. Incidentally, the cathode performance evaluated by means of galvanostatic technique is slightly different from the results of CV measurements, which is probably because the redox reactions observed in CV measurements involve the overpotential due to the kinetic reasons. Figure 5c shows XRD profiles after discharge/charge and compositional changes determined by energy-dispersive X-ray (EDX) spectroscopy analysis. The discharged sample for XRD analysis was made by holding the electrode at 2.0 V vs. LiRE for 12 hours. As shown in Figure 5c (upper panel), a rocksalt phase is formed after discharge (see dashed blue lines), whose lattice constant is similar to those of CoO and MgO, while there are no diffraction peaks corresponding to those of the wurtzite ZnO. The composition after discharge was determined to be Mg:Zn:Co = 0.55:0.95:2 by EDX analysis (see inset in Figure 5c). These results indicate that this is not the conversion reaction to form each oxide (e.g., ZnO, MgO, and CoO), but the Mg^{2+} insertion reac-
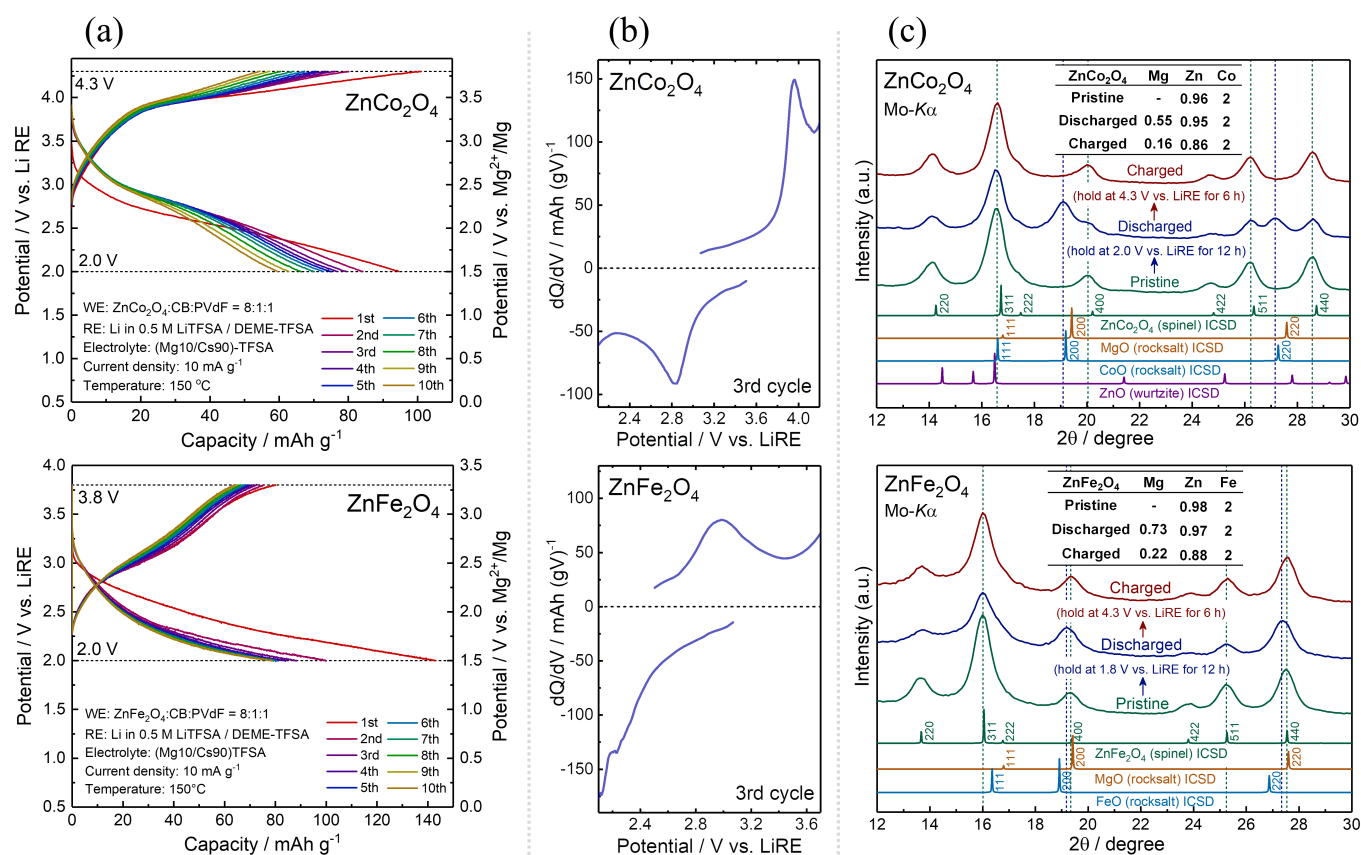
Fig. 5 (a) Cathode performance of $ZnCo_2O_4$ (upper) and $ZnFe_2O_4$ (lower) at 150 °C, where the first discharge was performed without any precharge process. (b) Differential capacity plots for $ZnCo_2O_4$ (upper) and $ZnFe_2O_4$ (lower) at the third cycle. (c) XRD profiles of $ZnCo_2O_4$ (upper) and $ZnFe_2O_4$ (lower) after discharge/charge. The insets show the results of EDX analysis for the same samples after XRD measurements.

tion to form $Mg_xZnCo_2O_4$ with the rocksalt structure. Because no peaks appeared except for the 200_R and 220_R peaks (and the 111_R peak that is hardly identified) from the generated phase, it is considered that the cations are disordered in the rocksalt structure. Although Zn prefers tetrahedral coordination, it was reported that a metastable cubic rocksalt structure can be formed under the coexistence with Mg.[36,37] The formation of such a relatively unstable rocksalt phase would improve the recoverability to the spinel structure with Mg extraction, whereas the gain of the Gibbs free energy would be slightly reduced. Besides, the electrical conductivity in the formed rocksalt phase is expected to be increased by using Zn compared with the case of Mg-based spinel oxides, because ZnO is a well-known n-type semiconductor,[38,39] whereas MgO is an insulator; the replacement of Mg with Zn would result in the increase of electron carrier concentration, as well as the decrease of band gap.[36,37] As seen in Figure 5a, there is a large difference between the theoretical and practical capacity (216 mAh g^{-1} and ~100 mAh g^{-1} in the first discharge, respectively). The resultant rocksalt phase on the surface of particles would decreases the practical capacity, for Mg diffusion in the close-packed phase is expected to be more sluggish than that in the spinel phase; actually, such a core–shell-like structure was found for $MgCo_2O_4$ after Mg insertion (Figure S14).

After charging, the generated rocksalt phase almost completely

reverts to the initial spinel structure as shown by the red profile in Figure 5c (upper panel), which supports the structural reversibility of bulk $ZnCo_2O_4$ with Mg insertion/extraction in the early cycle. Based on the result of NEB (Figure 2b), the activation energy for Mg (~450 meV) is much smaller than that for Zn (~600 meV). Thus, Mg should be preferentially extracted by charging compared with Zn in terms of the bulk diffusion. Figure S15 shows the activation probability ratio of Zn/Mg ions in the spinel host evaluated by the Boltzmann probability. At the temperature of 150 °C, the probability ratio of Zn/Mg ions is estimated to be as low as 0.0163, which suggests that the diffusion of Mg is dominant compared to that of Zn. However, the coextraction of Zn on charging would be facilitated especially on the surface of the particles; actually, the result of EDX analysis after charging indicates that Zn is also extracted to some extent along with Mg extraction (see inset in Figure 5c). It is expected that such compositional changes can be controlled by lowering operating temperature, which would suppress Zn extraction in terms of the Boltzmann probability as shown in Figure S15.

The discharge capacities of $ZnCo_2O_4$ gradually fade to ~60% within 10 cycles from the initial discharge. Although the degradation mechanism has not been clarified, it is considered that its large volume change in discharge/charge is one reason for the deterioration of cyclability. As shown in Figure 5c (upper panel),

there is a large difference between the angles of the 220_R peak (ca. 28.6 degrees) observed in the discharged sample and the 440_S peak (ca. 27.2 degrees) from the spinel phase. This indicates that there is a large lattice misfit of ~5% between the spinel and rocksalt structures ($a_{spinel} \simeq 8.14$ Å and $a_{rocksalt} \simeq 8.55$ Å), and its volume change amounts to as high as ~16%. The bulk modulus of Co-based spinel oxides is estimated to be about 160 GPa by *ab initio* calculation. If the elastic strain is simply assumed to be 8% for each phase, the hydrostatic pressure due to the coherent strain amounts to be about 13 GPa. Such a large volume change can cause the fractures of particles and electric contact loss during cycling, which can degrade the practical capacity. In addition, the strain energy can increase the overpotential for Mg insertion into spinel oxides; actually, the voltage drop due to the strain energy is estimated to be of the order of 0.1 V in this case (see details in Supporting Section S3). Thus, as is established in the field of lithium ion batteries,[40–42] suppressing the volume change in discharge/charge process would be a key strategy to achieve the improvement of the cyclability as well as the suppression of overpotential.

As shown in Figure 5a (lower panel), the capacity fade was markedly suppressed in the case of $ZnFe_2O_4$. A considerable cause of such the improved cycle property would be the substantial decrease of the volume change. In the XRD profile of the discharged sample, the intensity of diffraction peaks from the spinel structure, such as the 220_S, 311_S, and 511_S peaks, decreases with no peak shifts (lower panel in Figure 5c). This indicates that the volume fraction of the spinel mother phase is decreased with the insertion of Mg. Besides, the formation of a rocksalt phase is suggested by the shifts of the peaks at around 19 and 27.5 degrees (see dashed blue lines), which correspond to 200_R and 220_R, respectively. These small peak shifts to lower angles indicate that the formed rocksalt phase has slightly larger lattice size compared to the initial spinel phase, or almost spinel phase may be kept in that the Mg^{2+} and Zn^{2+} ions located around 8a sites after Mg insertion. Thus, the above results suggest that $ZnFe_2O_4$ can be seen as a nearly zero-strain cathode material. The obtained XRD profile after charging is very similar to that of the pristine sample, which indicates that the formed rocksalt phase successfully reverts to the spinel structure with Mg extraction. The composition after the discharge by holding the potential at 1.8 V vs. LiRE were determined to be Mg:Zn:Fe = 0.73:0.97:2 by EDX analysis. If the two-phase reaction of the stoichiometric $Zn_1Fe_2O_4$ (spinel) and $Mg_1Zn_1Fe_2O_4$ (rocksalt) is assumed, the molar fraction of rocksalt phases should be ~70% after discharge; however, the profile of the discharged sample suggests that there remains a larger amount of spinel phase. The above results suggest that there is a single-phase compositional region of $Mg_xZn_1Fe_2O_4$ with spinel-based structure before the spinel-to-rocksalt transition occurs. Actually, the dQ/dV plot (lower panel in Figure 5b) also indicates that there is a single-phase region in the range of about 2.5–3.0 V vs. LiRE. Therefore, the improved cyclability of $ZnFe_2O_4$ would be attributed to such a gradual phase change in discharge/charge. Incidentally, the irreversible discharge capacities continuously observed in Figure 5a would come from the reductive decomposition of the electrolyte.
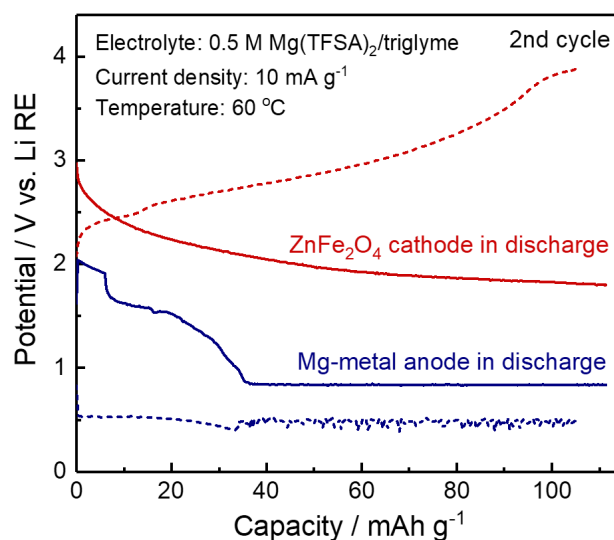

Fig. 6 Discharge/charge curves of $ZnFe_2O_4$ cathode and Mg-metal anode at the second cycle in 0.5 M Mg(TFSA)$_2$/triglyme electrolyte at 60 °C. The solid and dashed lines correspond to the electrode potentials in discharge and charge processes.

Finally, a prototype cell consisting of $ZnFe_2O_4$ cathode and Mg-metal anode was constructed by using an ether-based electrolyte of 0.5 M Mg(TFSA)$_2$/triglyme at 60 °C.[43] The redox potential of Mg^{2+}/Mg in this electrolyte was determined to be approximately in the range of 0.6–0.8 V vs. LiRE (Figure S17). As shown in Figure 6, $ZnFe_2O_4$ cathode successfully worked even at the relatively low temperature of 60 °C. Although the capacity fade was still observed with cycling (Figure S17), the above result suggests that $ZnFe_2O_4$ cathode can be used with such the conventional organic solvent-based electrolyte. As for the Mg-metal anode, it is considered that Mg deposition occurs in the charge process with the potential of ca. 0.5 V vs. LiRE (i.e., approximately −0.2 V vs. Mg^{2+}/Mg), however, the behavior of Mg dissolution was unstable especially at the early stage in the discharge process and there observed a large overpotential of ~1.5 V. This indicates that Mg-metal anode was readily passivated in the electrolyte. Such the large overpotential for Mg dissolution would be decreased by using Cl-containing electrolytes,[34,44–47], while the corrosive nature of Cl ions can be harmful to the practical use. Thus, the development of halogen-free electrolytes that are compatible with both Mg-metal anode and spinel-oxide cathode is expected to establish practical MRBs.

What Facilitates Inverse Rocksalt-to-Spinel Transition?

We schematically illustrate the roles of Zn in the spinel–rocksalt transition in Figure 7, based on the discussion using Figure 2b. In contrast to Ni that prefers octahedral coordination, Zn strongly prefers the tetrahedral coordination due to the covalent bonds with O ions (Figure 2d). This readily invokes that pushing-out of Zn^{2+} ions from tetrahedral 8a sites to octahedral 16c sites is energetically laborious; however, the rocksalt phase was resultingly formed after discharge, especially, for $ZnCo_2O_4$ (upper panel in
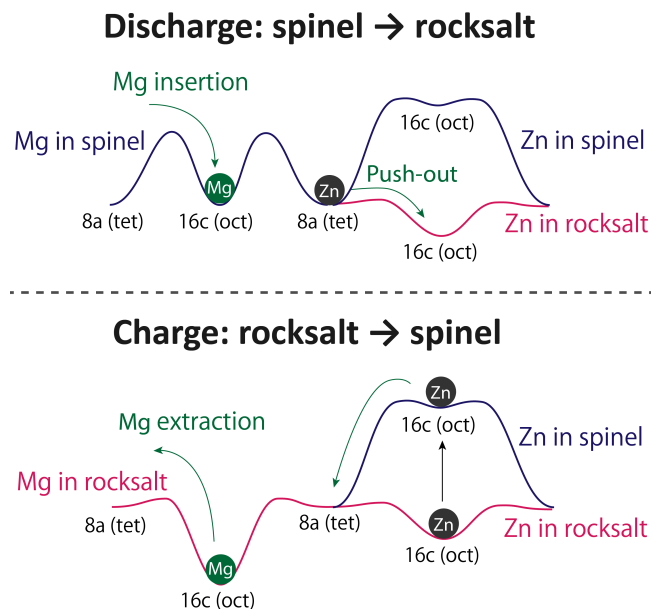
Discharge: spinel → rocksalt

Charge: rocksalt → spinel

Fig. 7 Schematic illustration showing the role of Zn in the spinel–rocksalt transition. Mg^{2+} insertion into 16c vacant sites would cause instability of Zn^{2+} ions at 8a sites in the discharge process (upper panel). In the charge process, Zn^{2+} ions would readily revert back to 8a sites to form the spinel structure along with Mg extraction (lower panel).

Figure 5c). This is probably because Mg^{2+} insertion into the octahedral 16c sites causes instability of Zn^{2+} ions on the tetrahedral 8a sites due to the electrostatic repulsion.[6] Consequently, Zn^{2+} ions are pushed out to adjacent 16c sites along with Mg insertion to form the rocksalt phase (upper panel in Figure 7). When Mg^{2+} ions are extracted in the charge process, Zn^{2+} is expected to readily revert to 8a sites, because the activation energy for Zn^{2+} ions from 16c sites to 8a sites in the spinel host is expected to be substantially small based on the results of the NEB calculation (Figure 2b and lower panel in Figure 7). Actually, the formed rocksalt phase almost completely reverts to the initial spinel structure after charging (Figure 5c). Thus, utilizing the metal cations such as Zn that prefer tetrahedral coordination for A cation in the spinel AB_2O_4 is considered to be a key strategy for improving the reversibility in the spinel–rocksalt transition. In addition, the flat energy profile of ion hopping for Zn^{2+} in $ZnCo_2O_4$ (Figure 2b) satisfies the condition of fast-ion diffusion driven by concerted migrations with multiple ions.[48] Therefore, it is expected that concerted migrations with two kinds of cations, i.e. Mg^{2+} and Zn^{2+} in this case, decrease the activation energy for diffusion in spinel hosts, as in the case of Mg–Li dual-ion battery system,[49,50] and we plan further studies on this issue in the near future.

CONCLUSION

In conclusion, we have revealed that stabilizing spinel structure by utilizing Zn that prefers tetrahedral coordination can improve the reversibility in the spinel–rocksalt transition. By computational studies, we have proven that Zn^{2+} prefers tetrahedral 8a site due to the formation of covalent bonds with O 2p orbital, while it becomes relatively ionic if located at octahedral 16c site. Actually, nanocrystals with basically normal spinel structure can

be obtained for $Zn(Co/Fe)_2O_4$, although Ni-based compositions tend to form rocksalt-like defective structures. In the electrochemical measurements at 150 °C, Zn-based spinel oxides enable facile Mg insertion/extraction with enhanced reversibility compared to Ni-based ones. By means of XRD analysis, we have made sure that Zn-based spinel oxides transform to the rocksalt structure with Mg insertion, and they can readily revert to the spinel structure with Mg extraction. Although the volume expansion in the spinel-to-rocksalt transition amounts to be as high as 16% for $ZnCo_2O_4$, it keeps nearly zero strain for $ZnFe_2O_4$ upon Mg insertion/extraction processes. Consequently, $ZnFe_2O_4$ exhibits the significantly improved cyclability in discharge/charge measurements at 150 °C. This work will provide fundamental guidelines for designing advanced spinel-oxide cathode materials to achieve high-performance multivalent batteries.

METHODS

Computational Details

First-principles density functional theory (DFT) calculations were performed using Vienna ab-initio simulation package (VASP) utilizing the projector augmented-wave (PAW) method and plane-wave basis set. A generalized gradient approximation (GGA)-type exchange-correlation functional developed by Perdew, Burke, and Ernzernhof and modified for solid materials (PBEsol) was used. For crystal structure relaxation and evaluation of total electron energies, on-site Coulomb correction (GGA + U) was used to describe the localized electronic states in Co 3d orbital. U was set to 3.4 eV for the Co 3d states according to literature.[51]

Synthesis

Nanocrystalline powder samples of $A(Co/Fe)_2O_x$ (A = Zn, Ni) were synthesized by an inverse coprecipitation method.[15] An aqueous solution of metallic nitrate salts was added dropwise into a solution of Na_2CO_3 at 70 °C to obtain a precursor. The details of the solution for each composition are listed in Table S4. The obtained precursor was ball-milled after vacuum drying, and then calcinated in air at 350 °C for two hours. The primary particle size of Zn-based spinel oxides was found to be ~10 nm (Figure S5) by using HAADF-STEM, and the secondary particle size was 1–10 μm due to the aggregation (Figure S4).

Electrochemical Measurements

Electrochemical measurements were performed using a galvanostat/potentiostat (Biologic, VSP-300 and VMP-3). A three-electrode beaker-type cell was constructed inside a glove box with Ar atmosphere, whose dew point was below −70 °C. The cell was set in an Al block heated by a hot plate to keep the temperature of the electrolyte at 150 °C. Mg ribbons used as the counter electrodes were polished with sand papers inside the glove box prior to use. A Li^+/Li system was used for the reference electrode, where a lithium metal was immersed in the solution of 0.5 M LiTFSA/DEME-TFSA (DEME: N,N-diethyl-N-methyl-N-(2-methoxyethyl) ammonium) separated from the main bath by a glass tube with a ceramic filter. Schematic illustration of the experimental setup is shown in Figure S18. (Mg10/Cs90)TFSA elec-

trolyte used for electrochemical measurements was prepared by mixing battery-grade $Mg(TFSA)_2$ (Kishida Chemical) and CsTFSA (Morita Chemical Industry) at 150 °C. As for CV measurements, composite electrodes were prepared from the mixture of spinel oxides, carbon black, and PTFE binder in a weight percent of 50:45:5. It is noted that such a large amount of carbon can enhance the electrochemical activity of spinel oxides. The mixture for each compound was pressed on an Al-mesh current collector, where the loading of spinel oxides onto each electrode was ca. 1 mg with an electrode area of 0.25 cm^{-2}. The electrode without any spinel oxide was prepared by mixing carbon black and PTFE in a weight ratio of 9:1. Galvanostatic discharge/charge performance and structural change of Zn-based spinel oxides were examined for the composite electrodes prepared by coating the mixtures of spinel oxides, carbon black, PVdF in a weight ratio of 8:1:1 on current collectors with mass loading of ca. 2 mg cm^{-2}. Al current collector was used for preparing samples for XRD measurements after discharging and charging because of its ease of handling and inexpensiveness, while Pt current collector was used for galvanostatic discharge/charge measurements to avoid the possibility of corrosion. $Mg(TFSA)_2$/triglyme electrolyte was prepared by mixing $Mg(TFSA)_2$ salt and triglyme solvent (99%, Tokyo Chemical Industry) that was pre-treated with 3A molecular sieves overnight. The discharge/charge performance of the prototype cell with 0.5 M $Mg(TFSA)_2$/triglyme was obtained by using a three-electrode beaker-type cell with the same Li-based reference electrode stated above.

Materials Characterization

Powder XRD measurements were performed by using an X-ray diffractometer (Rigaku, SmartLab) with Mo $K\alpha$ radiation. Discharged/charged samples were rinsed with tetrahydrofuran (THF) for several hours and then stripped from the current collectors to enclose glass capillaries whose diameter is 0.5 mm, and measured in the transmission geometry at room temperature. XANES measurements were performed at a synchrotron radiation facility, SPring-8. Scanning electron microscope (SEM) observation and EDX analysis were carried out using a scanning electron microscope (JEOL, JSM-IT200) with an acceleration voltage of 15 kV. STEM samples were prepared by suspending spinel powders on molybdenum-mesh grids covered by a thin perforated carbon, and HAADF-STEM imaging was made by using a spherical-aberration corrected microscope (JEOL, JEM-ARM200F) operated at 200 kV.

Acknowledgements

Author Contributions

K.S. and T.I. conceived and designed the experiments. T.A., M.H., R.E.W., and M.N. performed computational studies: GA, Monte Carlo, and NEB techniques. Y.K. and F.O. conducted the calculation of the equilibrium potentials. K.S. carried out the materials synthesis, electrochemical studies, and materials characterization. N.L.O. performed STEM observation. K.K. and T.I. oversaw the project. K.S., M.N., and T.I. wrote the manuscript. All authors contributed to discussions and revisions of the manuscript.

Notes and references

1 J. B. Goodenough and K. Park, *J. Am. Chem. Soc.*, 2013, **135**, 1167–1176.

2 D. Aurbach, Z. Lu, A. Schechter, Y. Gofer, H. Gizbar, R. Turgeman, Y. Cohen, M. Moshkovich and E. Levi, *Nature*, 2000, **407**, 724–727.

3 D. Aurbach, Y. Cohen and M. Moshkovich, *Electrochem. Solid-State Lett.*, 2001, **4**, A113–A116.

4 M. Matsui, *J. Power Sources*, 2011, **196**, 7048–7055.

5 J. Muldoon, C. B. Bucur and T. Gregory, *Chem. Rev.*, 2014, **114**, 11683–11720.

6 S. Okamoto, T. Ichitsubo, T. Kawaguchi, Y. Kumagai, F. Oba, S. Yagi, K. Shimokawa, N. Goto, N. Doi and E. Matsubara, *Adv. Sci.*, 2015, **2**, 1500072.

7 T. Ichitsubo, S. Okamoto, T. Kawaguchi, Y. Kumagai, F. Oba, S. Yagi, N. Goto, T. Doi and E. Matsubara, *J. Mater. Chem. A*, 2015, **3**, 10188.

8 T. Kamiyama, K. Haneda, T. Sato, S. Ikeda and H. Asano, *Solid State Commun.*, 1992, **81**, 563–566.

9 M. J. Akhtar, M. Nadeem, S. Javaid and M. Atif, *J. Phys.: Condens. Matter*, 2009, **21**, 405303.

10 K. Krezhov and P. Konstantinov, *J. Phys.: Condens. Matter*, 1993, **5**, 9287–9294.

11 R. M. Rojas, D. Kovacheva and K. Petrov, *Chem. Mater.*, 1999, **11**, 3263–3267.

12 P. W. Menezes, A. Indra, A. Bergmann, P. Chernev, C. Walter, H. Dau, P. Strasser and M. Driess, *J. Mater. Chem. A*, 2016, **4**, 10014.

13 C. Pan, R. G. Nuzzo and A. A. Gewirth, *Chem. Mater.*, 2017, **29**, 9351–9359.

14 Y. Noda, K. Nakano, H. Takeda, M. Kotobuki, L. Lu and M. Nakayama, *Chem. Mater.*, 2017, **29**, 8983–8991.

15 S. Yagi, Y. Ichikawa, I. Yamada, T. Doi, T. Ichitsubo and E. Matsubara, *Jpn. J. Appl. Phys.*, 2013, **52**, 025501.

16 H. Shiiba, M. Nakayama and M. Nogami, *Solid State Ionics*, 2010, **181**, 994–1001.

17 M. Liu, Z. Rong, R. Malik, P. Canepa, A. Jain, G. Ceder and K. A. Persson, *Energy Environ. Sci.*, 2015, **8**, 964–974.

18 M. Nakayama, M. Kaneko and M. Wakihara, *Phys. Chem. Chem. Phys.*, 2012, **14**, 13963–13970.

19 R. D. Shannon, *Acta Crystallogr., Sect. A*, 1976, **32**, 751–767.

20 J. F. Marco, J. R. Gancedo and M. Gracia, *J. Solid State Chem.*, 2000, **153**, 74–81.

21 J. F. Marco, J. R. Gancedo, M. Gracia, J. L. Gautier, E. I. Ríos,

H. M. Palmer, C. Greaves and F. J. Berry, *J. Mater. Chem.*, 2001, **11**, 3087–3093.

22 J. Li, S. Xiong, Y. Liu, Z. Ju and Y. Qian, *ACS Appl. Mater. Interfaces*, 2013, **5**, 981–988.

23 E. J. W. Verwey and E. L. Heilmann, *J. Chem. Phys.*, 1947, **15**, 174–180.

24 K. Tsukimura, S. Sasaki and N. Kimizuka, *Jpn. J. Appl. Phys.*, 1997, **36**, 3609–3612.

25 Q. Wei, J. Li and Y. Chen, *J. Mater. Sci.*, 2001, **36**, 5115–5118.

26 V. Šepelák, I. Bergmann, A. Feldhoff, P. Heitjans, F. Krumeich, D. Menzel, F. J. Litterst, S. J. Campbell and K. D. Becker, *J. Phys. Chem. C*, 2007, **111**, 5026–5033.

27 S. Greenwald, S. J. Pickart and F. H. Grannis, *J. Chem. Phys.*, 1954, **22**, 1597.

28 C. Pan, R. Zhang, R. G. Nuzzo and A. A. Gewirth, *Adv. Energy Mater.*, 2018, **8**, 1800589.

29 Q. D. Truong, M. K. Devaraju, P. D. Tran, Y. Gambe, K. Nayuki, Y. Sasaki and I. Honma, *Chem. Mater.*, 2017, **29**, 6245–6251.

30 V. G. Tsirelson, A. S. Avilov, Y. A. Abramov, E. L. Belokoneva, R. Kitaneh and D. Feil, *Acta Cryst.*, 1998, **B54**, 8–17.

31 W. L. Roth, *J. Phys. Chem. Solids*, 1964, **25**, 1–10.

32 H. Guo, J. Chen, W. Weng, Q. Wang and S. Li, *Chemical Engineering Journal*, 2014, **239**, 192–199.

33 M. Oishi, T. Ichitsubo, S. Okamoto, S. Toyoda, E. Matsubara, T. Nohira and R. Hagiwara, *J. Electrochem. Soc.*, 2014, **161**, A943–A947.

34 K. Shimokawa, H. Matsumoto and T. Ichitsubo, *J. Phys. Chem. Lett.*, 2018, **9**, 4732–4737.

35 T. Ichitsubo, S. Yagi, R. Nakamura, Y. Ichikawa, S. Okamoto, K. Sugimura, T. Kawaguchi, A. Kitada, M. Oishi, T. Doi and E. Matsubara, *J. Mater. Chem. A*, 2014, **2**, 14858–14866.

36 S. Choopun, R. D. Vispute, W. Yang, R. P. Sharma, T. Venkatesan and H. Shen, *Appl. Phys. Lett.*, 2002, **80**, 1529–1531.

37 X. Chen and J. Kang, *Semicond. Sci. Technol.*, 2008, **23**, 025008.

38 K. I. Hagemark, *J. Solid State Chem.*, 1976, **16**, 293–299.

39 F. Oba, M. Choi, A. Togo and I. Tanaka, *Sci. Technol. Adv. Mater.*, 2011, **12**, 034302.

40 T. Ohzuku, A. Ueda and N. Yamamota, *J. Electrochem. Soc.*, 1995, **142**, 1431–1435.

41 T. Wada, T. Ichitsubo, K. Yubuta, H. Segawa, H. Yoshida and H. Kato, *Nano Lett.*, 2014, **14**, 4505–4510.

42 T. Ichitsubo, S. Yukitani, K. Hirai, S. Yagi, T. Uda and E. Matsubara, *J. Mater. Chem.*, 2011, **21**, 2701–2708.

43 T. Fukutsuka, K. Asaka, A. Inoo, R. Yasui, K. Miyazaki, T. Abe, K. Nishio and Y. Uchimoto, *Chem. Lett.*, 2014, **43**, 1788–1790.

44 F. Bertasi, C. Hettige, F. Sepehr, X. Bogle, G. Pagot, K. Vezz, E. Negro, S. J. Paddison, S. G. Greenbaum, M. Vittadello and V. D. Noto, *ChemSusChem*, 2015, **8**, 3069–3076.

45 C. Liao, N. Sa, B. Key, A. K. Burrell, L. Cheng, L. A. Curtiss, J. T. Vaughey, J.-J. Woo, L. Hu, B. Panab and Z. Zhangb, *J. Mater. Chem. A*, 2015, **3**, 6082–6087.

46 I. Shterenberg, M. Salama, H. D. Yoo, Y. Gofer, J.-B. Park, Y.-K. Sun and D. Aurbach, *J. Electrochem. Soc.*, 2015, **162**, A7118–A7128.

47 N. Sa, B. Pan, A. Saha-Shah, A. A. Hubaud, J. T. Vaughey, L. A. Baker, C. Liao and A. K. Burrell, *Appl. Mater. Interfaces*, 2016, **8**, 16002–16008.

48 X. He, Y. Zhu and Y. Mo, *Nat. Commun.*, 2017, **8**, 15893.

49 H. Li, T. Ichitsubo, S. Yagi and E. Matsubara, *J. Mater. Chem. A*, 2017, **5**, 3534.

50 H. Li, N. L. Okamoto, T. Hatakeyama, Y. Kumagai, F. Oba and T. Ichitsubo, *Adv. Energy Mater.*, 2018, **8**, 1801475.

51 A. Jain, G. Hautier, S. P. Ong, C. J. Moore, C. C. Fischer, K. A. Persson and G. Ceder, *Phys. Rev. B*, 2011, **84**, 045115.